

## A TWO-DIMENSIONAL MAGNETOHYDRODYNAMICS SCHEME FOR GENERAL UNSTRUCTURED GRIDS

ELI LIVNE<sup>1</sup>, LUC DESSART<sup>2</sup>, ADAM BURROWS<sup>2</sup>, CASEY A. MEAKIN<sup>2</sup>

*Accepted to Ap.J.*

### ABSTRACT

We report a new finite-difference scheme for two-dimensional magnetohydrodynamics (MHD) simulations, with and without rotation, in unstructured grids with quadrilateral cells. The new scheme is implemented within the code VULCAN/2D, which already includes radiation-hydrodynamics in various approximations and can be used with arbitrarily moving meshes (ALE). The MHD scheme, which consists of cell-centered magnetic field variables, preserves the nodal finite difference representation of  $\text{div}(\mathbf{B})$  by construction, and therefore any initially divergence-free field remains divergence-free through the simulation. In this paper, we describe the new scheme in detail and present comparisons of VULCAN/2D results with those of the code ZEUS/2D for several one-dimensional and two-dimensional test problems. The code now enables two-dimensional simulations of the collapse and explosion of the rotating, magnetic cores of massive stars. Moreover, it can be used to simulate the very wide variety of astrophysical problems for which multi-D radiation-magnetohydrodynamics (RMHD) is relevant.

*Subject headings:* magnetohydrodynamics, multi-dimensional radiation hydrodynamics, supernovae

### 1. INTRODUCTION

Magnetic fields play a role, sometimes pivotal, in the evolution and dynamics of astrophysical objects. These include, but are not limited to, molecular clouds, protostars, stellar and planetary dynamos, pulsars, jets from active galactic nuclei, the solar wind, solar flares, the Earth's and Sun's magnetosheaths, and, importantly, accretion disks of all kinds. To investigate these environments theoretically has often required multi-dimensional simulation tools that in the past have incorporated the relevant physics only to varying degrees. The *ideal* MHD (magnetohydrodynamic) approximation, in which it is assumed the electrical conductivity of the fluid is “infinite” and, therefore, that the magnetic flux is frozen in the matter, is a very good one in many environments in the Universe and obviates the necessity to solve separate Boltzmann equations with microscopic couplings for the various charged components.

Recently, core-collapse supernova explosions and gamma-ray bursts have been added to the list of astrophysical sites in which magnetic fields might play an important role. In this paper, we describe a new 2.5-dimensional MHD algorithm (now incorporated into the radiation hydrodynamic code VULCAN/2D) that maintains the divergence-free character of the B-field to machine precision and applies to general structured and unstructured grids. We were motivated in developing this new capability by the intriguing possibility that magnetic fields might play a dynamical role in the mechanism of gamma-ray bursts and, possibly, in the explosions of a subset of core-collapse supernovae, as well as by an interest in the origin of pulsar and magnetar B-fields. Nevertheless, the new code can be used for a much wider set of problems, since along with rotation and magnetic fields in the *ideal* MHD approximation it also incorporates multi-group transport (in both the multi-angle  $S_n$  and flux-limited diffusion approximations) and a general gravity solver.

The possibility of hydromagnetic driving of supernova explosions was first explored quantitatively by LeBlanc & Wilson (1970). Using numerical simulations that were then the state-of-the-art, they showed that the combination of rapid rotation and strong magnetic fields in the pre-collapse core could lead to the formation of bipolar jets in the post-bounce configuration. In that picture, magnetic fields convert rotational energy into the jet energy via the pinch effect. The old simulations of LeBlanc & Wilson, however, suffered from crude spatial resolution and did not incorporate important developments in the physics of nuclear matter and in the neutrino-matter interaction. They employed gray transport and obtained rather weak explosions near  $\sim 10^{50}$  ergs. After this pioneering work, with few exceptions (Bisnovatyi-Kogan et al. 1976; Meier et al. 1976; Symbalisty 1984), the possible role of magnetic fields in powering or enabling supernova explosions took a back seat to other promising mechanisms. However, recently the subject of hydromagnetic interactions during core collapse has been revived by a number of investigators (Akiyama et al. 2003; Ardeljan et al. 2005; Yamada & Sawai 2004; Kotake et al. 2004; Ohnishi, Kotake, & Yamada 2005; Akiyama & Wheeler 2005; Proga 2005; Wilson, Mathews, & Dalhed 2005; Thompson, Quataert, & Burrows 2005; Moiseenko et al. 2006; Uzdensky & MacFadyen 2006ab; Masada, Sano, & Shibata 2006), who have investigated the potential of magnetic stresses, magnetic buoyancy, magnetic collimation, magnetic dissipation, and the magnetorotational instability (MRI, Balbus & Hawley 1991; Akiyama et al. 2003; Pessah & Psaltis 2005; Pessah, Chan & Psaltis 2006; Obergaulinger, Aloy, & Müller 2006; Etienne, Liu, & Shapiro 2006) to power explosion. In addition, the possibility that magnetic fields generated during black hole or neutron star formation might form energetic jets in the context of gamma-ray bursts,

<sup>1</sup> Racah Institute of Physics, The Hebrew University, Jerusalem, Israel

<sup>2</sup> Department of Astronomy and Steward Observatory, The University of Arizona, Tucson, AZ 85721

X-ray flashes, collapsars (MacFadyen & Woosley 1999), and hypernovae is receiving increasing attention (e.g., Mizuno et al. 2004). Furthermore, the potential role of magnetic winds in powering explosions, or secondary explosions, and in spinning down the nascent neutron star or magnetar is now being actively studied (Thompson, Chang, & Quataert 2004; Bucciantini et al. 2006; Metzger, Thompson, & Quataert 2006). In all these scenarios, rapid rotation and the growth of strong magnetic fields due to compression, winding, and/or the MRI during the dynamical phases of core collapse play essential roles. Whether progenitors boast the requisite rotation and initial seed fields remains to be determined (Heger et al. 2004; Heger, Woosley, & Spruit 2005), but an interesting subset surely must.

To date, there has been a great deal of MHD code development in astrophysics, mainly focused on simulating turbulent magnetic molecular clouds, accretion disks, AGN jets, solar and stellar dynamos, and solar plasmas, but lately also on the question of gamma-ray bursts and supernovae. Stone & Norman (1992ab) developed the ZEUS suite of codes that employs the method of characteristics (MOC) to properly address MHD waves and incorporates the constrained transport (CT) method (Evans & Hawley 1988) to handle the divergence condition on the B-field. It includes gray radiation transport using a short-characteristics method. Dai and Woodward (1994) developed an MHD Riemann solver and extended the piecewise parabolic method (PPM) to multidimensional MHD equations. They also presented a PPM variant that exactly preserves the conservation laws of magnetohydrodynamics together with the divergence-free condition (Dai & Woodward 1998). Gardiner & Stone (2005) have followed ZEUS/MHD with a dimensionally-unsplit, 2nd-order, Godunov, grid-based code (Athena) that combines the piecewise parabolic method (PPM) for spatial reconstruction and the corner transport upwind (CTU) method of Colella (1990) for time-advancing multi-dimensional hydro with the CT method for divergence preservation. Their numerical focus has been on making the CTU method compatible with both constrained transport and the finite-volume philosophy of PPM in the unsplit context. The result is an accurate and conservative MHD code with great potential to address astrophysical problems. Smooth-particle hydrodynamics (SPH) codes have recently been augmented to include magnetic fields, using divergence cleaning techniques (Price & Monaghan 2005; Ziegler, Dolag, & Bartelmann 2006) and have been employed to study, among other 3D problems, the merger of binary neutron stars (Price & Rosswog 2006). Divergence cleaning techniques have been criticized *vis à vis* staggered-mesh, divergence-free formulations (Balsara & Kim 2004) for artificially imposing post-facto cleaning methods to ensure  $\text{div}B = 0$ , but the approach is still useful for exploratory investigations. Aloy et al. (1999ab) have developed a sophisticated special-relativistic, axisymmetric MHD code that incorporates as algorithmic elements finite-volume, Godunov, directional splitting, constrained transport, and an HLL-type solver. Using a similar code, Obergaulinger et al. (2006) have recently investigated the MRI in the axisymmetric core-collapse context.

There are now several general-relativistic MHD codes that promise to set the standard for astrophysical GRMHD simulations in the future. Shibata & Sekiguchi (2005) have constructed a GRMHD code that features fully conservative numerical algorithms, dynamic space-times, and the constrained transport method. Noble et al. (2006) have built a conservative GRMHD code employing approximate Riemann solvers and a variant of constrained transport. Anninos, Fragile, & Salmonson (2005) have produced the GRMHD code, COSMOS++, that, while it also assumes a fixed background space-time, has unstructured grids. COSMOS++ is non-Godunov, uses artificial viscosity, uses finite-volume discretization, and has an AMR mode.

Despite all these recent developments in computational MHD and enormous progress in computing power and in numerical techniques, there is still no single code today that can simulate radiation-magnetohydrodynamics (RMHD) in full, mainly because a multi-angle, multi-group transport code is expensive, even in 2D. In this paper, we present a modest step toward such a code by reporting a new MHD scheme, incorporated into the already operational multi-group radiation hydrodynamics code VULCAN/2D (Livne 1993; Livne et al. 2004). Using multi-group, flux-limited diffusion we have obtained and recently published an interesting new explosion mechanism for core-collapse supernovae (Burrows et al. 2006ab). We have also explored accretion-induced rotational collapse (Dessart et al. 2006a), convection in protoneutron stars (Dessart et al. 2006b), the angle-dependence of the neutrino field and neutrino heating on rotation rate (Walder et al. 2005), the mapping between initial and final spins in the core-collapse context (Ott et al. 2006a), and the gravitational radiation signatures of multi-D supernovae (Ott et al. 2006b). There are several basic advantages of VULCAN/2D over other codes (together with some drawbacks) which enable the code to perform in difficult situations. One basic feature of VULCAN/2D is its ability to use unstructured grids, which in principle can efficiently cover any domain. For example, polar grids become singular at the center of a star and Cartesian grids have difficulty resolving the center, while at the same time covering the entire star. In VULCAN/2D, we construct a grid by merging an inner curved rectangular with an outer polar grid. The resulting grid resolves the entire star with no singularity. In order to maintain this capability we have designed our MHD scheme for unstructured grids, having arbitrarily-shaped (but convex) quadrilateral cells. Another approach has been taken by Ardeljan et al. 2000, who use a 2D grid composed of triangles only, that also avoids the singularity of polar grids.

In this paper, we report on the new MHD technique and present a number of test problems that demonstrate the ability of the code to simulate 2D magnetohydrodynamics problems with both toroidal and poloidal fields. The paper is constructed as follows. In §2, we describe in several subsections the basic equations and the finite-difference methodology for arbitrary geometry (§2.1), the Lagrangean case (§2.1.1), and the Eulerian case (§2.1.2). We continue in §2.2 with a discussion of the implementation in axially-symmetric geometries (§2.2) and follow with a discussion of the method for evolving the toroidal component with rotation (§2.2.1). We end §2 with a few words on necessary modifications to the Courant/CFL condition and boundary conditions (§2.2.2). Section 3.1 presents one-dimensional test problems and §3.2 presents two-dimensional tests, some of them are new. For some of the test problems the magnetic stresses are comparable to the pressure stresses. The associated tables and figures support our conclusion

(§4) that the automatically divergence-conserving MHD scheme we have implemented for general unstructured grids in our RMHD code VULCAN/2D provides competitive and reasonably accurate solutions to the dynamic equations of MHD in the Newtonian regime.

## 2. THE MHD FINITE-DIFFERENCE SCHEME

In this paper we do not consider gravity, and therefore, omit gravity terms from the equations. We also omit here all possible interactions between matter and radiation. This physics, very relevant to the core-collapse problem, is already included in VULCAN/2D and has been reported in several papers (Burrows et al. 2006ab; Ott et al. 2006ab, Dessart et al. 2006ab). The MHD equations for incompressible flow in Lagrangean coordinates are (Landau & Lifshitz 1960; Chandrasekhar 1961):

$$\frac{d\rho}{dt} + \rho \nabla \cdot \mathbf{v} = 0 \quad (1)$$

$$\rho \frac{d\mathbf{v}}{dt} = -\nabla p + \frac{1}{4\pi} (\nabla \times \mathbf{B}) \times \mathbf{B} \quad (2)$$

$$\frac{de}{dt} = -p \frac{d}{dt} \left( \frac{1}{\rho} \right) \quad (3)$$

$$\frac{d}{dt} \left( \frac{\mathbf{B}}{\rho} \right) = \left( \frac{\mathbf{B}}{\rho} \right) \cdot \nabla \mathbf{v}. \quad (4)$$

Here,  $e$  is the specific energy per gram and  $p(\equiv p(\rho, e, Y_e))$  is the pressure, given by the equation of state for a given density,  $\rho$ , internal specific energy per gram,  $e$ , and electron fraction,  $Y_e$  (the mean number of electrons per baryon). The Lagrangean time derivative  $\frac{d}{dt}$  can be translated to the laboratory-frame by the transformation  $\frac{d}{dt} = \frac{\partial}{\partial t} + \mathbf{v} \cdot \nabla$ .

The majority of current numerical schemes for hydrodynamics, including ours, use cell-centered variables for the construction of finite-difference approximations to the fluid equations. But unlike Godunov-type schemes, like PPM, VULCAN/2D uses staggered differencing where the acceleration and velocity are computed at cell nodes rather than at cell centers. In such staggering schemes the acceleration is computed by integrating the pressure times the normal over the surface of a control volume around each node. Therefore, we seek a scheme in which the magnetic field is also cell-centered, so that the contribution of the magnetic stress to acceleration can be handled in a similar fashion. This approach is different, for example, from the choices made in MOC-CT schemes (Stone & Norman 1992b), where the magnetic field variables are face-centered (component  $B_i$  is face-centered in the  $i$ -direction, but cell-centered in the perpendicular direction). We do not calculate Lorentz forces directly but rather compute the magnetic stress forces from the conservative form of the equations of motion. This is achieved using standard integration schemes, as is done for example in Ardeljan (2000). One advantage of our approach is the exact conservation of momentum through the simulation. In VULCAN/2D, we use the Cartesian coordinates  $(x, y)$  in the planar case and the cylindrical coordinates  $(r, z)$  in the axisymmetric case. With these choices of coordinate systems, our scheme preserves linear momentum by construction, ( $p_x, p_y$  in the planar case,  $p_z$  in the cylindrical case), and, in the latter case, angular momentum as well. We shall discuss the magnetic acceleration in more detail in section 2.2, where the cylindrical case is presented.

### 2.1. Differencing the Field Equations: Basic Approach for Arbitrary Geometry

Our field equation incorporates the *flux-freezing principle* used in Stone & Norman (1992b). For a given surface,  $S$ , enclosed by a closed loop,  $C$ , we define the flux:

$$\Phi = \int \int_S \mathbf{B} \cdot \mathbf{n} ds. \quad (5)$$

If the surface moves with some arbitrary *grid velocity*  $\mathbf{v}_g$  the temporal derivative of  $\Phi$  is given by

$$\frac{D\Phi}{Dt} = \oint_C (\mathbf{v} - \mathbf{v}_g) \times \mathbf{B} dl. \quad (6)$$

Here, the time derivative is taken along the trajectory  $\frac{d\mathbf{x}}{dt} = \mathbf{v}_g$ . We can utilize eq. (6) to evolve a cell-centered B-field in both Lagrangean and Eulerian schemes in the following way. Take, for example, the two-dimensional planar case, where a cell is some arbitrarily-shaped, convex, quadrilateral in the  $(x, y)$  plane. In order to evolve the field in time, according to the flux-freezing principle, we need to define two control surfaces in that cell (the number of control surfaces must be equal to the number of field components). There are several ways of constructing such control surfaces inside a given cell. We considered two such ways – first, connecting opposite mid-edge centers and second, connecting diagonals of two opposite nodes. For each such choice we can construct a simple scheme for the evolution of the magnetic field. However, the *diagonal scheme* has been found to be more stable, while at the same time obeying the divergence-free condition of the magnetic field in a very elegant way. Therefore, we shall focus on this choice in the rest of the paper.

#### 2.1.1. The Lagrangean Case

Ignoring for now the toroidal component of the field,  $B_\phi$ , the field is described by its two poloidal cell-centered components  $B_x, B_y$ . By writing two finite-difference approximations of eq. (6) for the two surfaces one gets two linear equations for the two field components. Let us consider first the Lagrangean case, where  $\mathbf{v}_g = \mathbf{v}$  and the right-hand-side of eq. (6) vanishes. Denote the two components of the two surfaces by  $\Delta_{x,i}$  and  $\Delta_{y,i}$ ,  $i = 1, 2$ . Also, denote variables at the beginning of the timestep by superscript  $n$  and variables at the end of the timestep by superscript  $n + 1$ . The discretization of eq. (6) in this case yields the following two linear equations for the magnetic field at the end of the timestep:

$$S_{x,1}^{n+1} B_x^{n+1} + S_{y,1}^{n+1} B_y^{n+1} = S_{x,1}^n B_x^n + S_{y,1}^n B_y^n \quad (7)$$

$$S_{x,2}^{n+1} B_x^{n+1} + S_{y,2}^{n+1} B_y^{n+1} = S_{y,2}^n B_x^n + S_{y,2}^n B_y^n. \quad (8)$$

The geometrical factors  $S_{x,i}, S_{y,i}$  are the components of the vector  $\mathbf{n}ds$ .

$$S_{x,i} = -\Delta_{y,i} \quad (9)$$

$$S_{y,i} = +\Delta_{x,i}. \quad (10)$$

It is easy to show that a divergence-free field remains divergence-free if we define a finite difference *node-centered* approximation for the divergence. From the divergence theorem, one gets the approximation

$$\text{div}(\mathbf{B})(P) \approx \int_S \mathbf{B} \cdot \mathbf{n}ds/V \quad (11)$$

where  $P$  is a grid node,  $S$  is a closed surface surrounding that point and  $V$  is the volume contained inside  $S$ . For our *diagonal scheme* the surface  $S$  is composed of the four diagonals surrounding  $P$  (see Fig. 1), and, therefore, the integral in eq. (11) is unchanged when the fields in the four relevant cells are evolved by eqs. (7)–(10).

### 2.1.2. The Eulerian Case

In the more general case, where  $\mathbf{v}_g \neq \mathbf{v}$ , the right hand side of eq. (6) represents advection of the B-field across the grid and does not vanish. We shall focus on the more common Eulerian case, where  $\mathbf{v}_g = 0$ . For each of our two surfaces we now have to compute the right hand side of eq. (6), and by this obtain two linear equations for the new cell-centered components of the field. To do this we need to extrapolate field values from cell centers to the four nodes of each cell. Note that for our *diagonal scheme* the divergence-free condition still holds throughout the evolution, because the advection terms cancel out in the integration of eq. (11) over a closed loop. This is true regardless of the *nodal*-field values. However, for reasons of stability and accuracy, these nodal values must be carefully defined according to monotonicity principles. This is a crucial step where the scheme is different from current MOC-CT schemes, which rely on one-dimensional flux-splitting in each direction. Our unstructured grid, which is certainly not orthogonal, requires more complex extrapolation in order to ensure accuracy and stability.

The Eulerian form of our difference scheme for the cell-centered components yields the following two linear equations:

$$S_{x,1}^{n+1} B_x^{n+1} + S_{y,1}^{n+1} B_y^{n+1} = S_{x,1}^n B_x^n + S_{y,1}^n B_y^n + \Delta t [B_x v_y - B_y v_x]_1 \quad (12)$$

$$S_{x,2}^{n+1} B_x^{n+1} + S_{y,2}^{n+1} B_y^{n+1} = S_{y,2}^n B_x^n + S_{y,2}^n B_y^n + \Delta t [B_x v_y - B_y v_x]_2. \quad (13)$$

Here, the brackets  $[B_x v_y - B_y v_x]_i$  stand for the difference between the enclosed expression on the two edges of diagonal  $i$ . The accuracy and stability of the scheme depend upon the exact definition of the nodal values of the magnetic field, while the velocity values are already node-centered. We, therefore, have to construct appropriate single-valued nodal field components from the cell-centered basic field, and those will be used in the advection terms on the right-hand-side of eqs. (12)–(13). The construction consists of the following steps:

- Compute spatial slopes for the field components according to van Leer's monotonic advection scheme (van Leer 1979).
- Extrapolate cell-centered values to the nodes using those slopes. Note that for one-dimensional advection of a scalar field this procedure provides a monotonic and second-order-accurate scheme when the advection is done upwind.
- There are now four nodal values for each field component at any internal node  $p$ , and each of them is related to one diagonal surface in one of the surrounding cells (see diagonals a,b,c,d in Fig. 2). Using the velocity vectors at that node define the *upwind parameter*  $\alpha_i = \cos(\mathbf{v}, \mathbf{T}_i)$  for each diagonal, where  $\mathbf{T}_i$  is a unit vector along the diagonal  $i$  pointing to the node  $p$ . According to the sign of this *upwind parameter* define the type of each surrounding surface to be *donor-type* if  $\alpha_i > 0$  and *acceptor-type* otherwise.
- Usually, there will be two *donor-type* surfaces (diagonals a and d in Fig. 2) and two *acceptor-type* surfaces (diagonals b and c in Fig. 2) at each (internal) node, but in regions where the grid is non-orthogonal this rule may not hold. Without loss of generality assume that surfaces 1, 2 are the two most *donor-type* surfaces out of the four surrounding surfaces, with nodal fields  $\mathbf{B}_1, \mathbf{B}_2$  and normals  $\mathbf{N}_1, \mathbf{N}_2$ , respectively. Construct the single-valued nodal field vector  $\mathbf{B}_p$  by solving the two linear equations  $\mathbf{B}_p \cdot \mathbf{N}_i = \mathbf{B}_i \cdot \mathbf{N}_i$ ,  $i=1,2$ , which imply that the

normal fluxes on the donor-type surfaces are the same when computed using  $\mathbf{B}_p$  or the primitive extrapolations  $\mathbf{B}_i$ .

The above algorithm deserves a few remarks. First, the choice of donor-type surfaces actually guarantees that the two chosen diagonals (surfaces) are not parallel, so that this construction is indeed possible. Secondly, the construction of the nodal magnetic vector from the donor-type normal components ensures that the new fluxes are kept bound through the advection step. This is essentially the heart of our generalization of van Leer's monotonic upwind scheme to the case of magnetic fluxes. Only minor changes are needed for boundary points and we omit discussion here of those details. Finally, the same algorithm is applicable for general nonzero *grid velocity*, which could be used in ALE simulations by VULCAN/2D.

## 2.2. Implementation in Axially-Symmetric Geometry

Let us use the common coordinates, cylindrical  $r, z, \phi$ , for the radial, axial, and azimuthal directions. Assuming axial symmetry the azimuthal derivative of any variable vanishes everywhere, but the toroidal components of the magnetic field and the azimuthal velocity do not vanish. We first present the equations of motion in a form suitable for discretization:

$$\rho \frac{dv_r}{dt} = \frac{1}{4\pi} [B_z (\frac{\partial B_r}{\partial z} - \frac{\partial B_z}{\partial r}) - \frac{1}{2} \frac{\partial B_\phi^2}{\partial r} - \frac{B_\phi^2}{r}] - \frac{\partial p}{\partial r} \quad (14)$$

$$\rho \frac{dv_z}{dt} = \frac{1}{4\pi} [\frac{1}{r} \frac{\partial (r B_r B_z)}{\partial r} + \frac{1}{2} \frac{\partial (B_z^2 - B_r^2 - B_\phi^2)}{\partial z}] - \frac{\partial p}{\partial z} \quad (15)$$

$$\rho \frac{d(rv_\phi)}{dt} = \frac{1}{4\pi} [\frac{1}{r} \frac{\partial (r^2 B_r B_\phi)}{\partial r} + \frac{\partial (r B_z B_\phi)}{\partial z}], \quad (16)$$

to be compared with Ardeljan et al. (2000) and chapter IX of Chandrasekhar (1961) for the incompressible inviscid case. The main reason for writing the magnetic terms in this form is that the equation for the axial momentum and the equation for the angular momentum have a conservative form. The difference scheme of VULCAN/2D preserves these conservation laws by construction. The impulse and acceleration at each grid point are obtained by integrating the above equations over the surface of a local control volume, a cell in the staggered grid, which surrounds the point. Thus, momentum conservation laws are preserved exactly by the finite-difference scheme, as the integration provides at each surface segment two forces which have equal magnitude and opposite direction. Since this technique is standard in hydrodynamical schemes which use staggered grids we omit further details. Note however that the radial momentum in cylindrical coordinates is not a conserved quantity.

Returning to the evolution of the magnetic field we first discuss the poloidal components ( $B_r, B_z$ ), while the evolution of the toroidal field will be described separately in §2.2.1. The numerical approximation of those equations is obtained from the flux-freezing principle in a way similar to the planar case. We first take a cell in the  $(r, z)$  plane with the two surfaces defined by the diagonals connecting opposite nodes. The cell represents a torus around the axis of symmetry and the surfaces are actually closed ring-like sheets centered around the axis of symmetry. In the Lagrangean case, the resulting two linear equations for  $(B_r, B_z)$  are then

$$S_{r,1}^{n+1} B_r^{n+1} + S_{z,1}^{n+1} B_z^{n+1} = S_{r,1}^n B_r^n + S_{z,1}^n B_z^n \quad (17)$$

$$S_{r,2}^{n+1} B_r^{n+1} + S_{z,2}^{n+1} B_z^{n+1} = S_{r,2}^n B_r^n + S_{z,2}^n B_z^n, \quad (18)$$

where the geometrical factors are

$$S_{r,i} = -2\pi r_i \Delta_{z,i} \quad (19)$$

$$S_{z,i} = +2\pi r_i \Delta_{r,i}, \quad (20)$$

$r_i$  being the radius at the center of each surface. We see that the only difference with the planar case is the factor of  $2\pi r$  multiplying each geometrical factor. Likewise, in the Eulerian case we get equations similar to eqs. (12)–(13) with appropriate  $2\pi r$  factors. Therefore, the numerical technique for evolving the poloidal field is almost identical to that in the planar case.

### 2.2.1. The Toroidal Component and Rotation

For the time evolution of the toroidal component we need an extra equation. In the pure Eulerian case, which is our most common case, the equation for the toroidal field takes the form

$$\frac{\partial B_\phi}{\partial t} = \frac{\partial}{\partial r} (B_r v_\phi - B_\phi v_r) + \frac{\partial}{\partial z} (B_z v_\phi - B_\phi v_z). \quad (21)$$

Using flux freezing again, we define an extra surface which extracts the toroidal field. This is just the rectangular image of the cell in the  $(r, z)$  plane. Integrating eq. (21) over this surface yields the desired equation. After integration, the right-hand-side gives edge-centered advection terms which we compute using the standard upwind van Leer scheme.

### 2.2.2. Boundary Conditions and Time Steps for MHD Problems

We employ an *explicit* version of VULCAN/2D hydro and, thus, must restrict the timestep according to stability constraints. We use the CFL condition (Courant & Friedrichs 1948) updated to account for the propagation of Alfvén and fast magnetosonic waves. In practice, we use

$$\Delta t < \min \left( \frac{\Delta x}{|v| + C_f} \right), \quad (22)$$

where  $|v|$  is the local velocity (accounting for any rotational component as well) and  $C_f$  is the fast-magnetosonic speed ( $C_f^2 = v_A^2 + C_s^2$ ), where  $v_A$  is the Alfvén speed and  $C_s$  the sound speed. Note that in core-collapse supernova simulations, incorporating modest initial magnetic fields does not reduce noticeably the time increment, which after bounce is of the order of a microsecond. VULCAN/2D can also operate in an implicit mode where the Courant condition for acoustic waves is removed. The MHD solver however is explicit in nature. This implies that, depending on the field strength, the timestep in future implicit simulations could be restricted by the speed of Alfvén waves.

As to boundary conditions, they can be rather complicated if one wishes to simulate general MHD problems in arbitrary geometries. Since we are interested mainly in the core-collapse problem, and problems of a similar nature around compact objects, we choose to sacrifice the general case in favor of the most simple treatment. In our current implementation, the dynamical region is embedded in a large enough ambient region where either practically nothing changes during the simulations, or the outer boundary is not allowed to move. Therefore, under those restricted assumptions, a divergence-free initial field remain stationary in the outer regions of the flow.

## 3. TEST PROBLEMS

A number of one-dimensional and two-dimensional test problems have been chosen to verify the code, in both planar and cylindrical geometries. We have computed some of the test problems suggested in Stone et al. (1992) and in Stone & Norman (1992b). We have also designed a few new test problems which are relevant to dynamical collapse. The results of each VULCAN/2D simulation are compared to a simulation done under identical conditions using the publicly available MHD code ZEUS/2D (Stone et al. 1992; Stone & Norman 1992b).

### 3.1. One-Dimensional Test Problems

In this section, we present one-dimensional planar and cylindrical test problems. For this purpose, we constructed a one-dimensional Lagrangean magnetohydrodynamic version, VULCAN/1D, based upon the MHD formalism outlined in this paper and upon the earlier work of Bisnovatyi-Kogan et al. (1976). VULCAN/1D is a variant that assumes that all the hydrodynamical and magnetic variables are functions of  $(r, t)$  alone. We use this Lagrangean code for testing our basic *flux freezing* approach in constructing the finite-difference scheme, and also for post comparisons between VULCAN/2D and VULCAN/1D. In most cases, the results of our VULCAN/2D (Eulerian) simulations are compared either to similar results obtained using VULCAN/1D (Lagrangean) or to those obtained using ZEUS/2D (Eulerian).

#### 3.1.1. Advection of a Magnetic Pulse

This problem addresses the one-dimensional advection of a pulse of transverse magnetic field in Cartesian geometry, following the procedure presented in Evans & Hawley (1988) and in Stone et al. (1992). The velocity is fixed and uniform throughout the grid and the exact solution is just a translation of the initial signal. The test probes the magnitude of the numerical dispersion and diffusion of the advection scheme employed in the MHD solver, that should operate exactly like the same advection scheme of a scalar field.

Our initial conditions are a one-dimensional grid of 500 zones, equally spaced to tile the  $x$ -direction from 0 to 100. We use a Courant number of 0.5 and the equation of state is that of an ideal gas. Density and pressure are set to a fixed value everywhere, a value which does not matter in practice since we perform pure advection. The velocity is unity everywhere, and we start with a non-zero transverse magnetic field between  $x = 10$  and  $x = 20$ . Boundary conditions are periodic. We run the simulation until this pulse has advected five times its initial width. We show in Fig. 3 the results for the ZEUS/2D simulations using the donor-cell scheme and the van Leer scheme and for simulations using VULCAN/2D. For comparison, we overplot the initial (square) pulse shifted along the  $x$ -direction by  $vt$ . VULCAN/2D results are very close to ZEUS/2D with the van Leer scheme (the two curves, essentially, overlapping). Given this good agreement, we do not investigate the distribution of the current density nor estimate errors as shown in Figs. 2–3 in Stone et al. (1992). As expected, van Leer’s scheme introduces a dramatic improvement of the results compared to donor cell. Another higher-order variant, the PPA scheme of ZEUS/2D, improves only a little on van Leer’s scheme, while introducing non-monotonic unphysical oscillations (not shown here).

#### 3.1.2. Brio-Wu Test Problem

The Brio-Wu test problem (Brio & Wu 1988) is a one-dimensional, planar, MHD Riemann problem. Analytic solutions to MHD Riemann problems are discussed in Ryu & Jones (1995). The particular Brio-Wu problem belongs to a subclass of *compound states*, where the analytic solution is ambiguous. We, therefore, compare our results to the numerical solution of ZEUS/2D. The  $x$ -range extends from 0 to 100, and the initial parameters on the two sides of the initial discontinuity at  $x = 50$  are:

$$\begin{cases} x \leq 50 : & \rho = 1.000, P = 1.0, B_x = 0.75, B_y = +1 \\ x \geq 50 : & \rho = 0.125, P = 0.1, B_x = 0.75, B_y = -1. \end{cases}$$

The equation of state is of an ideal gas with  $\gamma = 2$ . Boundary conditions are reflecting. To illustrate the behavior of VULCAN/2D *vis à vis* ZEUS/2D, we follow the same procedure found in Stone et al. (1992) and perform tests at different resolutions, assessing qualitatively and quantitatively the errors and how these vary with resolution. The Courant number for all simulations is set to 0.5.

First, in Fig. 4, we present the solution of the Brio-Wu problem at  $t = 10$  computed with VULCAN/2D (black) and ZEUS/2D with the van Leer scheme (red). The agreement seen in the graphs is excellent. For a quantitative comparison of ZEUS/2D with the van Leer scheme, VULCAN/2D, and the analytic Brio-Wu results, we log in Table 1 the values predicted by each for the density,  $\rho$ , the pressure,  $P$ , the velocities,  $V_x$  and  $V_y$ , and the B-field component,  $B_y$ . We provide these values at strategic locations in the fluid, which, from left to right, are the fast rarefaction (FR;  $x = 45$ ), the shock discontinuity (SC;  $x = 48$ ), the left and right sides of the contact discontinuity (CD<sub>l</sub> and CD<sub>r</sub>;  $x = 55$ ), the fast rarefaction (FR;  $x = 80$ ), as well as the left and right initial boundary values for reference.

Following Stone et al. (1992), using self-convergence testing, we now estimate errors and convergence rates for both ZEUS/2D and VULCAN/2D in this specific Brio-Wu test. The simulations presented in Fig. 4 were done with  $N = 512$  zones, uniformly spaced in the x-direction. We performed a series of similar calculations with different resolutions:  $N = 64, 128, 256, 1024$ , and 2048. We then calculated an  $L_1$  error norm defined by

$$L_1 = \left[ \frac{\int |\rho_{2N}(x) - \rho_N(x)| dx}{\int dx} \right], \quad (23)$$

where  $\rho_{2N}(x)$  ( $\rho_N(x)$ ) represents the density in the run with  $2N$  ( $N$ ) zones, both taken at  $t = 10$  and at the same location  $x$ . Note that here  $L_1$  is a density error norm and that it has the units of a density, rather than being dimensionless. Using this measure, we seek the rate at which the error varies with resolution, rather than the absolute level of that error. Having six levels of resolution, we compute  $L_1$  for five consecutive pairs and show the results in the left panel of Fig. 5. The convergence rate is similar for both simulations, i.e., ZEUS/2D with van Leer's scheme and VULCAN/2D.

Finally, we display in the right panel of Fig. 5 the relative density errors for the simulations at  $N = 256$  (broken) and  $N = 1024$  (solid) zones for VULCAN/2D (Black) and ZEUS/2D/van Leer (red). Stone et al. (1992) noted that such an MHD shock-tube test, with a sharp discontinuity, forces code accuracy to be first-order. Our comparisons between codes that are completely different in design provide an instructive look into code performance and the accuracy of the results generated.

### 3.1.3. Propagation of an Alfvén Wave in 1D

Here, we examine the propagation of a 1D Alfvén wave, defined as a transverse perturbation on a given constant field  $B_x = B_0$ , embedded in a homogeneous medium of constant density  $\rho$ . The solution of such a wave as a function of  $x$  is naturally (Landau & Lifshitz 1960):

$$v_y(x, t) = v_0 \cos(kx - \omega t) \quad (24)$$

$$B_y(x, t) = -\sqrt{4\pi\rho} v_y. \quad (25)$$

The perturbations  $v_y$  and  $B_y$  propagate along the  $x$  direction with the Alfvén speed  $v_A = \frac{B_0}{\sqrt{4\pi\rho}}$ . We evolve the solution at  $t = 0$  with  $k = 2$  in the interval  $[0, 2\pi]$  for five periods and compare the profiles at each integer period to the initial configuration. Table 2 lists the L1 error of  $B_y$  for various resolutions ( $N$ ) and 5 integer periods. As functions of resolution, our errors behave similarly to those presented in Table II of Toth (2000) for the traveling wave, and show a second-order rate of convergence. As a function of time, we observe a linearly growing error in each column in Table 2 due to the fact that our scheme, like most other schemes, is only first-order accurate in time. Moreover, in more realistic problems which involve advection and/or acoustic waves, second-order accuracy usually degrades to nearly first-order. This can be seen in Toth's Table II for the standing wave and in his Tables V-VIII, where the 7 tested schemes show a roughly first-order rate of convergence with spatial resolution.

### 3.1.4. Transport of Angular Momentum in a Rotating Disk

This one-dimensional problem in cylindrical geometry tests the evolution of a toroidal field, together with the transport of angular momentum in a differentially rotating disk. Here, we start with differential rotation in the radial direction and a corresponding radial magnetic field. This configuration is more typical of astrophysical problems than is employed in the *Braking of aligned rotators* problem of Stone et al. (1992). The stresses of the radial magnetic field transport angular momentum from the inner parts outward, evolving towards uniform rotation, while a toroidal field grows from zero to significant magnitude. Bisnovatyi-Kogan et al. (1976) suggested this mechanism for an MHD-driven supernova, but they need extremely strong initial fields to generate an explosion.

We first set an initial disk configuration in rotational equilibrium, where the centrifugal acceleration is balanced by pressure only, namely,

$$\frac{1}{\rho} \frac{\partial p}{\partial r} = r\omega^2(r). \quad (26)$$

Using an isentropic ideal gas with adiabatic index  $\gamma$ ,  $p = A\rho^\gamma$ , and a rotation law of the form

$$\omega(r) = \frac{\omega_0 L^2}{L^2 + r^2}, \quad (27)$$

one can integrate the hydrostatic equation to get the entire disk configuration as a function of the radius. We computed this test problem, with the parameters  $p(r=0, t=0) = 100$ ,  $\rho(r=0, t=0) = 1$ ,  $\gamma = 5/3$ ,  $\omega_0 = 10$  (in dimensionless units), using our one dimensional Lagrangean code VULCAN/1D and VULCAN/2D in the Eulerian mode. The radius of the disk is  $r_{max} = 10$  and the width of the initial rotation profile is  $L = r_{max}/4$ . In both simulations, we have used 500 radial zones and fixed, rigid, outer boundary conditions. Without a magnetic field the disk remains static and stable in both simulations, showing that the schemes do not introduce spurious numerical errors. For the real test we turn on a radial magnetic field of magnitude  $rB_r = 100$  and evolve the configuration until  $t=0.5$ . Figure 6 displays the toroidal field  $B_\phi$  (left) and the angular velocity at three times (0.0,0.3,0.5). The pluses, showing the results of VULCAN/2D, are plotted for only one fifth (100) of the zones in order not to hide the solid lines. The excellent agreement between the two codes lends credence to the accuracy and stability of our 2D Eulerian scheme, which is much more complicated than its 1D Lagrangean version.

### 3.2. Two-Dimensional Test Problems

There are only a few published dynamical test problems which are two-dimensional in nature. Therefore, we constructed a number of such problems, which are close to astrophysical problems in their dynamics, and compared the results of VULCAN/2D with those of ZEUS/2D. We focus on problems which involve supersonic flow and strong shock waves, rather than on steady-state problems like wind solutions. In the absence of analytic solutions code-to-code comparison is the only way to validate multi-dimensional simulations. However, such comparisons should be done with great care. In a few previous attempts, it was found that significant differences between codes persist even when high-order schemes are used with maximum available resolution. Examples are the ‘‘Santa Barbara Cluster Comparison Project’’ (Frenk et al. 1999), the ‘‘Richtmyer-Meshkov Instability Study’’ of Holmes et al. (1999) and the ‘‘Rayleigh-Taylor Instability Study’’ of the ‘‘Alpha-Group’’ (Dimonte et al. 2004). The differences between codes arise from the tendency of unstable flows to form smaller and smaller structures due to vorticity generation. Therefore, one can anticipate finding good agreement between two codes only on resolved structures, for which there are at least 10-12 grid zones. In other words, there should be no point-wise convergence in simulations of unstable flows in regions with small-scale fragmentation and shear (see also discussions by Calder et al. 2002). Consequently, self-convergence tests in the sense described in §3.1.2 are not a common practice in multi-dimensional simulation.

#### 3.2.1. Exploding Sphere/Blast Wave

This axisymmetric test problem consists of the expansion of a high pressure sphere embedded inside an ambient cloud with initially uniform  $B_z$  magnetic field. The specific setup used is (in normalized dimensionless units):

$$\begin{cases} 0.01 < R < 0.2 : & \rho = 100, P = 10^6, B_r = 0, B_z = 140 \\ 0.20 < R < 1.0 : & \rho = 1.0, P = 0.60, B_r = 0, B_z = 140, \end{cases}$$

where  $R$  is the spherical radius, and  $B_r$  and  $B_z$  refer to the cylindrical components of the magnetic field (spherical geometry is, however, used for the simulation). The problem was evolved with an ideal gas equation of state with  $\gamma = 5/3$  and the Courant number used is again 0.5. The spherical grid is logarithmically spaced in radius with  $nr$  zones between 0.01 and 1.0 and uniformly spaced in angle with  $nt$  zones between 0 and  $\pi$ . Boundary conditions are reflecting and the simulation is stopped before the blast wave hits the outer boundary.

We show in Fig. 7 a montage of the density (top-left panel), pressure (top-right panel), and the cylindrical  $r$  and  $z$  components of the magnetic field (bottom-left and bottom-right panels, respectively) at the final time  $t = 0.0035$  in a high-resolution simulation with  $nr = 280$  and  $nt = 240$ . Each panel is broken into two halves, with the VULCAN/2D results on the right and the ZEUS/2D results on the left. To give a better rendering of the dynamics and of the poloidal field morphology, we overplot velocity vectors (unsaturated; maximum length corresponds to a value of 165 or a physical length of 10% of the width of the display). Magnetic field lines are drawn starting from  $z = -0.95 r_{max}$ , equally spaced every  $0.1r_{max}$  in the horizontal direction. The different paths followed by these lines between the two sides are indicative of differences in the magnetic field computed by VULCAN/2D and ZEUS/2D. Overall, lines bunch up in the shock region where they accumulate due to flux freezing with the mass.

At the qualitative level, the agreement between the two codes is excellent. The colormaps of the components of the poloidal field show the compression of the vertical field  $B_z$  and the generation of the radial component due to flux freezing. Because the flow field of this problem is irrotational, we performed a resolution study in the sense described at the previous section. Since in this test problem there are only large-scale structures without shear we expect to see some kind of convergence. We show in Table 3 the results at the final time for the extrema of the density, pressure,



$V_r$ ,  $V_z$ ,  $B_r$ , and  $B_z$ . Figure 7 shows results for the highest-resolution simulation, while in Table 3 we give additional data for low resolution ( $nr = 71$  and  $nt = 61$ ) and medium-resolution ( $nr = 141$  and  $nt = 121$ ) tests. All quantities converge at higher resolution where they differ between the two codes by no more than a few percent. However, at low resolution, differences can be of the order of 20-30%. Note, however, that in general the low-resolution and medium-resolution values obtained by VULCAN/2D are closer to their high-resolution values than those obtained by ZEUS/2D. Using the highest resolution model as the reference model, the  $L_1$  error norm for the density (see discussion in the Brio-Wu test above) gives a value for the low- and medium-resolution simulations, respectively, of 0.42 and 0.22 for ZEUS/2D, 0.24 and 0.19 for VULCAN/2D. Overall, ZEUS/2D and VULCAN/2D compare well for this explosion test, both qualitatively and quantitatively.

### 3.2.2. Imploding Sphere

In this test, the initial spherically-symmetric configuration is split between an outer low-density, high-pressure shell and an inner high-density, low-pressure region. The entire domain is threaded by a uniform vertical field  $B_z$ . The initial setup is given by (in normalized dimensionless units):

$$\begin{cases} 0.04 < R < 0.8 : & \rho = 10, P = 1.00, B_r = 0, B_z = 40 \\ 0.80 < R < 2.0 : & \rho = 1.0, P = 1000, B_r = 0, B_z = 40. \end{cases}$$

The problem was evolved with an ideal gas equation of state with  $\gamma = 5/3$ , and in the highest resolution version, we employ  $nr = 360$  logarithmically-spaced radial zones and  $nt = 240$  uniformly-spaced angular zones on a full  $\pi$  sector. The initial configuration evolves so that the outer high-pressure region implodes, compressing the inner region right down to the inner boundary at  $R = 0.04$ , which then reexpands. The interaction of the magnetic field with the implosion leads to fragmentation of the shock wave and to the formation of many small-scale structures. The ratio of the gas pressure to the magnetic pressure ( $\beta$ ) reaches unity inside near bounce. Note that for such tests with ZEUS/2D a large latitudinal flow developed at mid-latitude in the inner-boundary “shell” promptly after the start of the simulation. We cured this anomaly in this otherwise static inner region by modifying the base boundary condition in ZEUS/2D to enforce a null latitudinal velocity in the ghost zones and in the first active zone.

In a first test, we computed the implosion without rotation, for which we show in Fig. 8 results for the density (top left), pressure (top right),  $B_r$  (bottom left) and  $B_z$  (bottom right) at time  $t = 0.05$  and in Fig. 9 at time  $t = 0.07$ . The shock bounces at the inner rigid surface shortly after  $t = 0.05$ , and we evolve the flow until  $t = 0.1$ . Even before shock bounce, a complex pattern is formed due to the interaction between the vertical magnetic field and the radially converging flow (Fig. 8). After bounce, the flow fragments on smaller scales and forms complex structures by non-radial shock interactions (Fig. 9). The two codes agree well on scales which are resolved by more than a few zones. Although VULCAN/2D is not designed to conserve energy exactly (with or without magnetic fields) the total energy in this simulation is conserved to an accuracy of  $\sim 0.2$  percent; the magnetic energy accounts for roughly 5 percent of the total. Both codes preserve accurately the left-right symmetry of  $B_z$  and the anti-symmetry of  $B_r$ . Those symmetries are seen in Fig. 8 and subsequent figures, but can best be rendered by the morphology of the poloidal field lines (top right panels of Figs. 8 and 9 and in the right panels of Figs. 10 and 11).

VULCAN/2D seems more dissipative than ZEUS/2D on the smallest scales and at sharp discontinuities. The slight differences at these smallest scales and at interfaces could be consequences of the fact that VULCAN/2D does not currently use any “sharpening” techniques on discontinuities. The agreement between the codes persists all the way to the end of the simulation at  $t = 0.1$  (not shown here). In Table 4, we present the integrated energy components at several times. We can see that the total energy is conserved at the same level of accuracy in the two codes. The agreement between separate components of the energy budget is also good, where the largest difference appears in the kinetic energy. Since this difference appears already at early times, and then remains roughly constant, we speculate that the origin of this difference is a different treatment of the initial shock wave that emerges from the large initial pressure discontinuity.

A second similar test uses the same initial input, but with initial rotation. The initial rotation speed is given by  $v_\phi(r) = \frac{\Omega_0 r}{1+(r/A)^2}$  and we choose  $\Omega_0 = 10$  and  $A = 0.5$  ( $r$  is the cylindrical radius). In Fig. 10, we present comparisons of the angular velocity  $\Omega$  (left column) and the toroidal magnetic field  $B_\phi$  (right column) before bounce ( $t = 0.05$ ; top row) and after bounce ( $t = 0.07$ ; bottom row). The initial field in this simulation is purely poloidal, so that the non-zero toroidal field stems from the winding of the poloidal component through differential rotation. The complex 2D configuration of the angular velocity leads to both positive and negative toroidal components of the magnetic field, depending on location (height above the inner boundary and hemisphere). Again, the agreement between the codes is good for all structures resolved by more than a few zones. In Table 5, we present the integrated energy components at the times used for the non-rotating case. The conservation of total energy and the agreement between different energy components are of the same quality as in the previous case. Note, however, that while VULCAN/2D preserves the total angular momentum exactly ZEUS/2D does not, though the deviation is only a few percent.

All simulations presented so far were set up with intermediate strength initial B-fields, and, indeed, comparable magnetic and gas pressures were obtained only transiently in the simulations, e.g., during the bounce epoch in the implosion test. To test the high B-field case, we repeated the high-resolution non-rotating implosion test discussed earlier, but this time increased the initial magnetic field magnitude from 40 to 120 and 300. The magnetic field pressure then dominates the gas pressure. We present in Fig. 11 a montage of colormaps of the density (left) and the

quantity  $\beta_{\text{plasma}} = P/(B^2/8\pi)$  (right), the ratio of thermal and magnetic pressures, for the cases with initial fields  $B_z = 120$  (top;  $t = 0.06$ ) and  $B_z = 300$  (bottom;  $t = 0.04$ ). Note how the material is more and more confined to motion along field lines as the field strength increases, preventing any perpendicular motion in the highest  $B_z$ -value case. Here, as before, differences are noticeable between VULCAN/2D and ZEUS/2D, for example in the extrema reached by the density and  $\beta_{\text{plasma}}$  (or the gas pressure and the magnetic field components), but overall the agreement is quite satisfactory. Simulations at high magnetic field strength imply large Alfvén speed and, thus, reduced timestep. Because such simulations are costly, we stopped those simulations earlier than the final times of the intermediate strength cases.

#### 4. CONCLUSIONS

We have developed an ideal MHD scheme for general unstructured grids in two dimensions, plus rotation. The scheme consists of flux freezing of cell-centered magnetic vectors in both Lagrangean and Eulerian realizations. For the Eulerian mode, we generalized the van Leer second-order advection scheme for cell-centered fluxes in a unique way. The scheme is now incorporated into the (Newtonian) radiation hydrodynamics code VULCAN/2D and can be used for future two-dimensional RMHD simulations of rotating core-collapse supernovae and the early phases of gamma-ray bursts, as well as for simulations of a variety of other multi-D RMHD astrophysical problems.

Via a number of one-dimensional and two-dimensional test problems, we find that the accuracy of the scheme is comparable to that of high-order MOC-CT schemes used, for example, in the code ZEUS/2D. It is, however, impossible to prove a *formal order of accuracy* for our scheme because it does not consist of one-dimensional sweeps. In actual test problems we see that VULCAN/2D is somewhat more dissipative on small, unresolved, scales than ZEUS/2D, but the agreement between the two codes on structures that are resolved by more than a few zones is good. The extra dissipation of VULCAN/2D is probably related to numerical details that are not related to the MHD scheme, and do not affect resolved scales. The MHD scheme is designed to conserve the nodal finite-difference representation of  $\text{div}(\mathbf{B})$  automatically to machine accuracy at all times. Moreover, it conserves linear and angular momenta in the axisymmetric cylindrical case.

We thank Mordecai Mac Low, Christian Ott, and Jeremiah Murphy for interesting discussions. This research was supported by The Israel Science Foundation (grant No. 805/04). We also acknowledge support from the Scientific Discovery through Advanced Computing (SciDAC) program of the DOE, under grants DE-FC02-01ER41184 and DE-FC02-06ER41452, and from the NSF under grant AST-0504947. This research used resources of the National Energy Research Scientific Computing Center, which is supported by the Office of Science of the U.S. Department of Energy under Contract No. DE-AC03-76SF00098. Finally, this research used resources of the NCCS at Oak Ridge National Laboratory, which is supported by the Office of Science of the Department of Energy under contract DE-AC05-00OR22725.

#### REFERENCES

- Akiyama, S., Wheeler, J.C., Meier, D.L., & Lichtenstadt, I. 2003, ApJ, 584, 954
- Akiyama, S. & Wheeler, J.C. 2005, ApJ, 629, 414
- Aloy, M.A., Ibañez, J.M., Martí, J.M., Gómez, J.-L., & Müller, E. 1999a, ApJ, 523, L125
- Aloy, M.A., Ibañez, J.M., Martí, J.M., & Müller, E. 1999b, ApJS, 122, 151
- Anninos, P., Fragile, P.C., & Salmonson, J.D. 2005, ApJ, 635, 723
- Ardeljan, N.V., Bisnovatyi-Kogan, G.S., & Moiseenko, S.G. 2000, A&A, 355, 1181,
- Ardeljan, N.V., Bisnovatyi-Kogan, G.S., & Moiseenko, S.G. 2005, MNRAS, 359, 333
- Balbus, S.A. & Hawley, J.F. 1991, ApJ, 376, 222
- Balsara, D.S. & Kim, J. 2004, ApJ, 602, 1079
- Bisnovatyi-Kogan, G.S., Popov, I.P., & Samokhin, A.A. 1976, Ap&SS, 41, 287
- Blondin, J.M., Mezzacappa, A., & DeMarino, C. 2003, ApJ, 584, 971
- Brio, M., & Wu, C.C. 1988, J. Comp. Phys., 75, 400
- Bucciantini, N., Thompson, T.A., Arons, J., Quataert, E., & Del Zanna, L. 2006, MNRAS, 368, 1717
- Burrows, A., Livne, E., Dessart, L., Ott, C.D., & Murphy, J. 2006, ApJ, 640, 878
- Burrows, A., Livne, E., Dessart, L., Ott, C.D., & Murphy, J. 2006, ApJ, 640, 878
- Calder, A.C. et al. 2002, ApJS, 143, 201
- Chandrasekhar, S. 1961, in “Hydrodynamic and Hydromagnetic Stability”, Oxford Univ. Press
- Colella, P. 1990, J. Comp. Phys., 87, 171
- Courant, R., & Friedrichs, K.O. 1948, in “Pure and Applied Mathematics”, New York: Interscience
- Dai, W. & Woodward, P.R. 1994, J. Comp. Phys., 111, 354
- Dai, W. & Woodward, P.R. 1998, ApJ, 494, 317
- Dessart, L., Burrows, A., Ott, C.D., Livne, E., Yoon, S.-Y., & Langer, N. 2006a, ApJ, 644, 1063
- Dessart, L., Burrows, A., Livne, E., & Ott, C.D. 2006b, ApJ, 645, 534
- Dimonte, G. et al. 2004, Phys. of Fluids, 16, 1668
- Evans, C.R. & Hawley, J.F. 1988, ApJ, 332, 659
- Etienne, Z.B., Liu, Y.T., & Shapiro, S.L. 2006, Phys. Rev. D, 74, 044030
- Foglizzo, T., Galletti, P. & Ruffert, M. 2005, A&A, 435, 397
- Frenk, C.S. et al. 1999, ApJ, 525, 554
- Gardiner, T.A. & Stone, J.M. 2005, J. Comp. Phys., 205, 509
- Heger, A., Woosley, S. E., Langer, N., & Spruit, H. C. 2004, IAU Symposium, 215, 591
- Heger, A., Woosley, S.E., & Spruit, H. 2005, ApJ, 626, 350 (astro-ph/0409422)
- Holmes, R.L., Dimonte, G., Fryxell, B.A., Gittings, M.L., Grove, J.W., Schneider, M., Sharp, D.H., Velikovich, A.L., Weaver, R.P., & Zhang, Q. 1999, J. Fluid Mech., 389, 55
- Kotake, K., Sawai, H., Yamada, S., & Sato, K. 2004, ApJ, 608, 391
- Landau, L.D. & Lifshitz, E.M. 1960, in “Electrodynamics of Continuous Media,” Pergamon Press
- LeBlanc, J.M., & Wilson, J.R. 1970, ApJ, 161, 541
- Livne, E. 1993, ApJ, 412, 634
- Livne, E., Burrows, A., Walder, R., Thompson, T.A., and Lichtenstadt, I. 2004, ApJ, 609, 277
- Masada, Y., Sano, T., & Shibata, K. 2006, accepted to ApJ(astro-ph/0610023)
- MacFadyen, A.I. & Woosley, S.E. 1999, ApJ, 524, 262
- Meier, D.L., Epstein, R.I., Arnett, W.D & Schramm, D.N., 1976, ApJ, 204, 869

- Metzger, B., Thompson, T.A., & Quataert, E. 2006, astro-ph/0608682
- Mizuno, Y., Yamada, S., Koide, S., & Shibata, K. 2004, ApJ, 606, 395
- Moiseenko, S.G., Bisnovatyi-Kogan, G.S., & Ardeljan, N.V. 2006, MNRAS, 370, 501
- Noble, S.C., Gammie, C.F., McKinney, J.C., & Del Zanna, L. 2006, ApJ, 641, 626
- Ohnishi, N., Kotake, K., & Yamada, S. 2005, astro-ph/0509765
- Obergaulinger, M., Aloy, M.A., & Müller, E. 2006, A&A, 450, 1107
- Ott, C.D., Burrows, A., Dessart, L., & Livne, E. 2006a, ApJ Suppl., 164, 130
- Ott, C.D., Burrows, A., Dessart, L., & Livne, E. 2006b, Phys. Rev. Lett., 96, 201102
- Pessah, M.E., & Psaltis, D. 2005, ApJ, 628, 879
- Pessah, M.E., Chan, C., & Psaltis, D. 2006, MNRAS, in press (astro-ph/0603178)
- Price, D.J. & Monaghan, J.J. 2005, MNRAS, 364, 384
- Price, D.J. & Rosswog, S. 2006, Science, 312, 5774
- Proga, D. 2005, ApJ, 629, 397
- Ryu, D., & Jones, T.W. 1995, ApJ, 442, 228
- Shibata, M. & Sekiguchi, Y. 2005, Phys. Rev. D, 72, 044014
- Stone, J.M., & Norman, M.L. 1992a, ApJS, 80, 753
- Stone, J.M., & Norman, M.L. 1992, ApJS, 80, 791
- Stone, J.M., Hawley, J.F., Evans, C.R., & Norman, M.L. 1992, ApJ, 388, 415
- Symbalisty, E.M.D. 1984, ApJ, 285, 729
- Thompson, T.A., Chang, P., & Quataert, E. 2004, ApJ, 611, 393
- Thompson, T.A., Quataert, E., & Burrows, A. 2005, ApJ, 620, 861
- Toth, G. 2000, J. of Comp. Phys., 161, 605
- Uzdensky, D.A. & MacFadyen, A.I. 2006a, ApJ, 647, 1192
- Uzdensky, D.A. & MacFadyen, A.I. 2006b, astro-ph/0609047
- Wilson, J.R., Mathews, G.J., & Dalhed, H.E. 2005, ApJ, 628, 335
- Walder, R., Burrows, A., Ott, C.D., Livne, E., Lichtenstadt, I., & Jarrar, M. 2005, ApJ, 626, 317
- Yamada, S., & Sawai, H. 2004, ApJ, 608, 907
- van Leer, B. 1979, J. Comp. Phys., 32, 101
- Ziegler, E., Dolag, K., & Bartelmann, M. 2006, Astronomische Nachrichten, 327, 607

TABLE 1  
VALUES OF SELECTED QUANTITIES FOR THE BRIO-WU TEST AT  $t = 10$ .

Variable	Source	Left	FR	SC	CD <sub>l</sub>	CD <sub>r</sub>	FR	Right
$\rho$	VULCAN/2D	1.0	0.664	0.839	0.704	0.242	0.116	0.125
	ZEUS/2D	1.0	0.660	0.840	0.699	0.250	0.116	0.125
	BW		0.676		0.697			
$P$	VULCAN/2D	1.0	0.441	0.719	0.505	0.505	0.086	0.1
	ZEUS/2D	1.0	0.435	0.712	0.501	0.501	0.086	0.1
	BW		0.457		0.516			
$V_x$	VULCAN/2D	0.0	0.663	0.485	0.596	0.596	-0.264	0.0
	ZEUS/2D	0.0	0.672	0.488	0.603	0.603	-0.279	0.0
	BW		0.637		0.599			
$V_y$	VULCAN/2D	0.0	-0.247	-1.19	-1.58	-1.58	-0.185	0.0
	ZEUS/2D	0.0	-0.251	-1.16	-1.58	-1.58	-0.196	0.0
	BW		-0.233		-1.58			
$B_y$	VULCAN/2D	1.0	0.568	-0.190	-0.537	-0.537	-0.892	-1.0
	ZEUS/2D	1.0	0.562	-0.195	-0.539	-0.539	-0.886	-1.0
	BW		0.585		-0.534			

NOTE. — Hydromagnetic variables at selected locations in the BW solution, which, from left to right, are the fast rarefaction (FR;  $x = 45$ ), the shock discontinuity (SC;  $x = 48$ ), the left and right sides of the contact discontinuity (CD<sub>l</sub> and CD<sub>r</sub>;  $x = 55$ ), the fast rarefaction (FR;  $x = 80$ ), as well as the left and right initial boundary values for reference (see Fig.4). Note how these values closely match.

TABLE 2  
L1 ERRORS IN  $B_y$  FOR THE ALFVÉN WAVE TEST

Periods	N=16	N=32	N=64	N=128
P=1	0.0086	0.0021	0.00054	0.00015
P=2	0.0171	0.0041	0.00106	0.00028
P=3	0.0256	0.0062	0.00158	0.00041
P=4	0.0339	0.0083	0.00210	0.00054
P=5	0.0423	0.0103	0.00262	0.00068

NOTE. — The value of N indicates the number of zones per wavelength

TABLE 3  
VALUES OF SELECTED QUANTITIES FOR THE EXPLOSION TEST AT  $t = 0.0035$ , USING LOW, MEDIUM, AND HIGH RESOLUTION.

Variable	Code	Low resolution		Medium resolution		High resolution	
		Min.	Max.	Min.	Max.	Min.	Max.
$\rho$	VULCAN/2D	1.00	3.53	1.0	4.48	1.0	5.4
	ZEUS/2D	1.02	2.83	0.99	4.12	0.97	5.3
$P$	VULCAN/2D	0.60	10157	0.6	10119	0.6	10525
	ZEUS/2D	2.18	7995	0.59	10186	0.57	10857
$V_r$	VULCAN/2D	-0.18	152.9	-0.15	157.6	-0.1	161.2
	ZEUS/2D	0.0	143.5	0.26	156.6	0.18	160.9
$V_z$	VULCAN/2D	-161.2	161.2	-164.0	164.0	-164.5	164.5
	ZEUS/2D	-146.3	146.3	-158.8	158.8	-164.3	164.3
$B_r$	VULCAN/2D	-160.7	160.7	-205.8	205.8	-214.0	214.0
	ZEUS/2D	-127.7	127.7	-189.3	189.3	-208.0	208.0
$B_z$	VULCAN/2D	-0.8	381.3	-3.18	405.9	-4.5	417.0
	ZEUS/2D	-7.8	331.1	-6.3	402.2	-8.6	420.0

TABLE 4  
ENERGY COMPONENTS IN THE HIGH-RESOLUTION NON-ROTATING IMPLOSION TEST.

Time	Code	$E_{kin}$	$E_{int}$	$E_{mag}$	$E_{rot}$	$J$	$E_{tot}$
0.	VULCAN	0.0	$4.705 \times 10^4$	$2.133 \times 10^3$	0.	0.	$4.918 \times 10^4$
	ZEUS	0.0	$4.705 \times 10^4$	$2.117 \times 10^3$	0.	0.	$4.916 \times 10^4$
0.03	VULCAN	$6.575 \times 10^2$	$4.625 \times 10^4$	$2.223 \times 10^3$	0.	0.	$4.913 \times 10^4$
	ZEUS	$6.954 \times 10^2$	$4.613 \times 10^4$	$2.216 \times 10^3$	0.	0.	$4.905 \times 10^4$
0.05	VULCAN	$6.598 \times 10^2$	$4.618 \times 10^4$	$2.270 \times 10^3$	0.	0.	$4.911 \times 10^4$
	ZEUS	$6.961 \times 10^2$	$4.605 \times 10^4$	$2.267 \times 10^3$	0.	0.	$4.902 \times 10^4$
0.07	VULCAN	$1.598 \times 10^2$	$4.658 \times 10^4$	$2.353 \times 10^3$	0.	0.	$4.910 \times 10^4$
	ZEUS	$1.881 \times 10^2$	$4.645 \times 10^4$	$2.364 \times 10^3$	0.	0.	$4.900 \times 10^4$
0.10	VULCAN	$6.247 \times 10^2$	$4.624 \times 10^4$	$2.215 \times 10^3$	0.	0.	$4.908 \times 10^4$
	ZEUS	$6.469 \times 10^2$	$4.611 \times 10^4$	$2.216 \times 10^3$	0.	0.	$4.898 \times 10^4$

TABLE 5  
ENERGY COMPONENTS IN THE HIGH-RESOLUTION ROTATING IMPLOSION TEST.

Time	Code	$E_{kin}$	$E_{int}$	$E_{mag}$	$E_{rot}$	J	$E_{tot}$
0.	VULCAN	0.0	$4.705 \times 10^4$	$2.133 \times 10^3$	$1.076 \times 10^2$	87.08	$4.929 \times 10^4$
	ZEUS	0.0	$4.705 \times 10^4$	$2.117 \times 10^3$	$1.076 \times 10^2$	87.08	$4.927 \times 10^4$
0.03	VULCAN	$6.199 \times 10^2$	$4.626 \times 10^2$	$2.222 \times 10^3$	$1.357 \times 10^2$	87.08	$4.923 \times 10^4$
	ZEUS	$6.546 \times 10^2$	$4.615 \times 10^2$	$2.214 \times 10^3$	$1.362 \times 10^2$	87.70	$4.916 \times 10^4$
0.05	VULCAN	$5.861 \times 10^2$	$4.617 \times 10^4$	$2.255 \times 10^3$	$1.988 \times 10^2$	87.08	$4.921 \times 10^4$
	ZEUS	$6.172 \times 10^2$	$4.606 \times 10^4$	$2.253 \times 10^3$	$2.021 \times 10^2$	88.68	$4.913 \times 10^4$
0.07	VULCAN	$1.693 \times 10^2$	$4.645 \times 10^4$	$2.323 \times 10^3$	$2.610 \times 10^2$	87.08	$4.920 \times 10^4$
	ZEUS	$1.869 \times 10^2$	$4.632 \times 10^4$	$2.332 \times 10^3$	$2.733 \times 10^2$	90.16	$4.912 \times 10^4$
0.10	VULCAN	$5.811 \times 10^2$	$4.623 \times 10^4$	$2.217 \times 10^3$	$1.600 \times 10^2$	87.08	$4.919 \times 10^4$
	ZEUS	$6.037 \times 10^2$	$4.611 \times 10^4$	$2.213 \times 10^3$	$1.737 \times 10^2$	93.10	$4.910 \times 10^4$

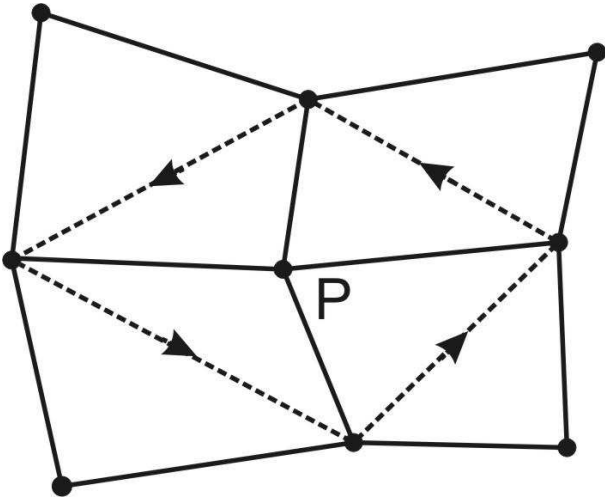


FIG. 1.— Scheme template: solid line quadrilaterals are grid cells. The dashed-line closed loop around  $P$  is the control surface for computing  $\text{div}(\mathbf{B})$  at  $P$ . In each cell there are two diagonals used to compute  $(B_r, B_z)$ .

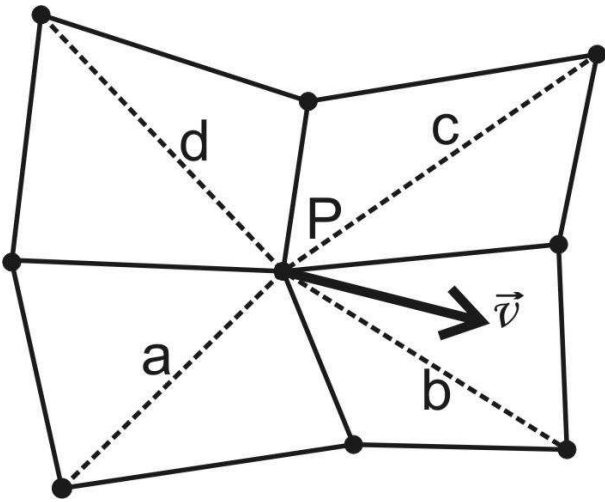


FIG. 2.— Template of the advection step: the velocity vector defines two *donor-type* diagonals (a,d) and two *acceptor-type* diagonals (b,c), according to the upwind stability criterion.

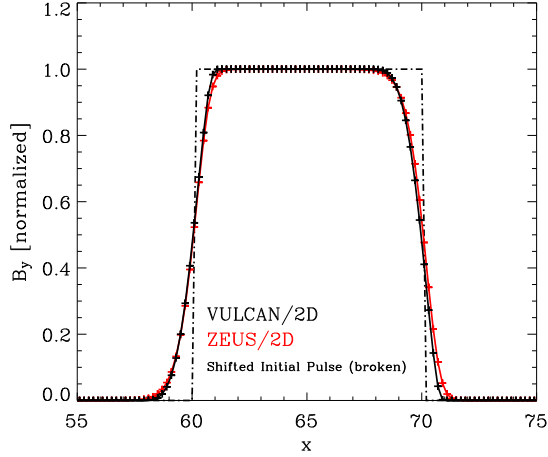


FIG. 3.— Illustration of the advected  $B_y$ -field for the pure advection test of a transverse magnetic pulse at  $t = 50$ , employing 500 zones, using the ZEUS code (green: Donor cell scheme; red: van Leer scheme) and VULCAN/2D (solid black). For comparison, we overplot the “exact” advection (translation) of the initial pulse (broken black).

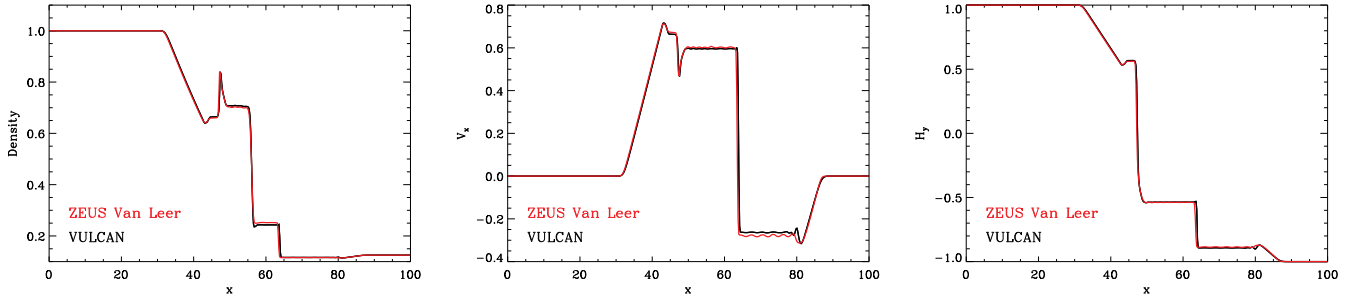


FIG. 4.— Illustration of the density (top), x-velocity (middle), and  $B_y$ -field (bottom) for the Brio-Wu test at  $t = 10$ , employing 512 zones, using VULCAN/2D (black) and ZEUS/2D (red).

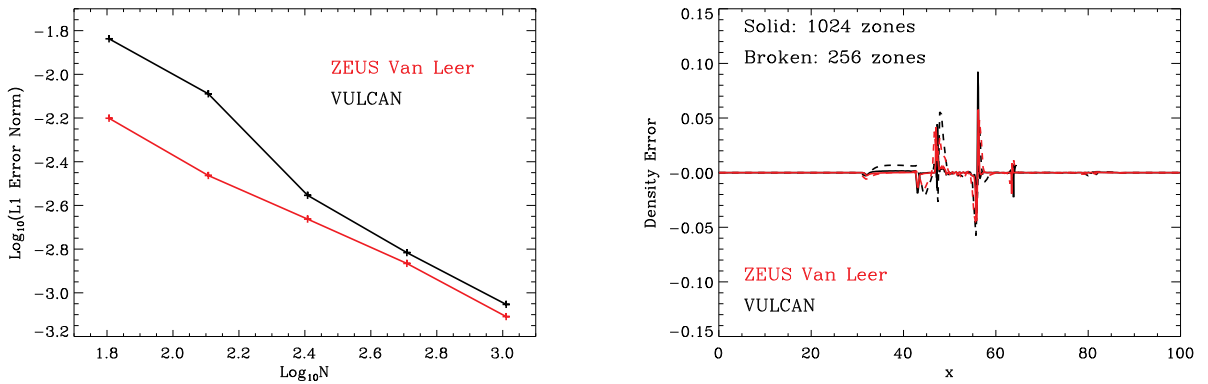


FIG. 5.— *Left*: Illustration of the  $L_1$  error norm computed on the density for the Brio-Wu test with VULCAN (black) and ZEUS/2D (red) as a function of the logarithm of the number of zones employed, *i.e.*  $N = 64, 128, 256, 512, 1024$ , and 2048.



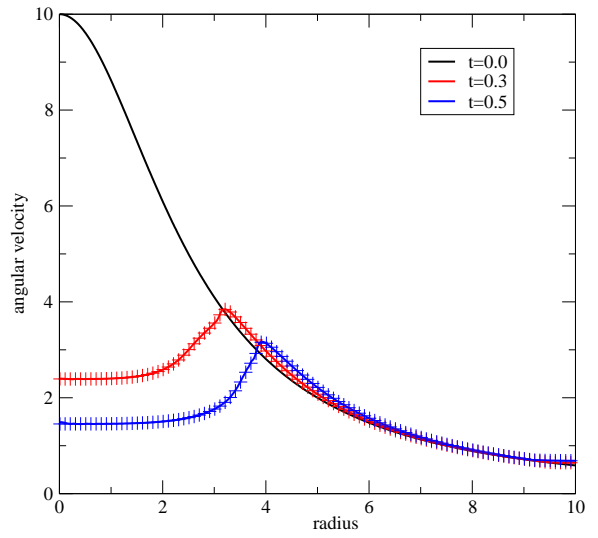
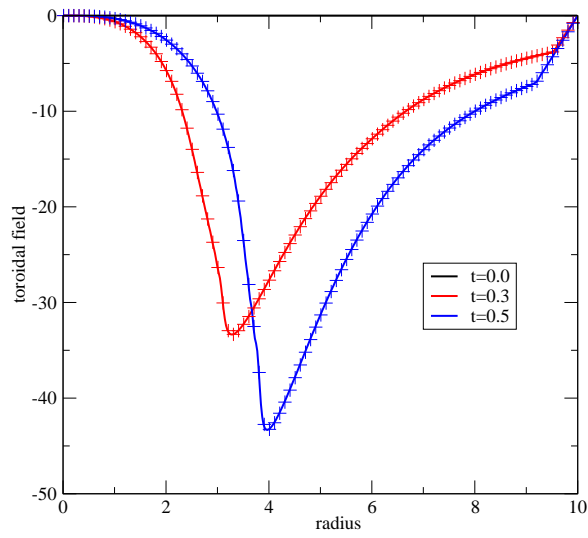


FIG. 6.— *Left:* The toroidal field  $B_\phi$ ; *Right:* The angular velocity  
 Solid lines - VULCAN/1D Lagrangean simulation, pluses - VULCAN/2D Eulerian simulation

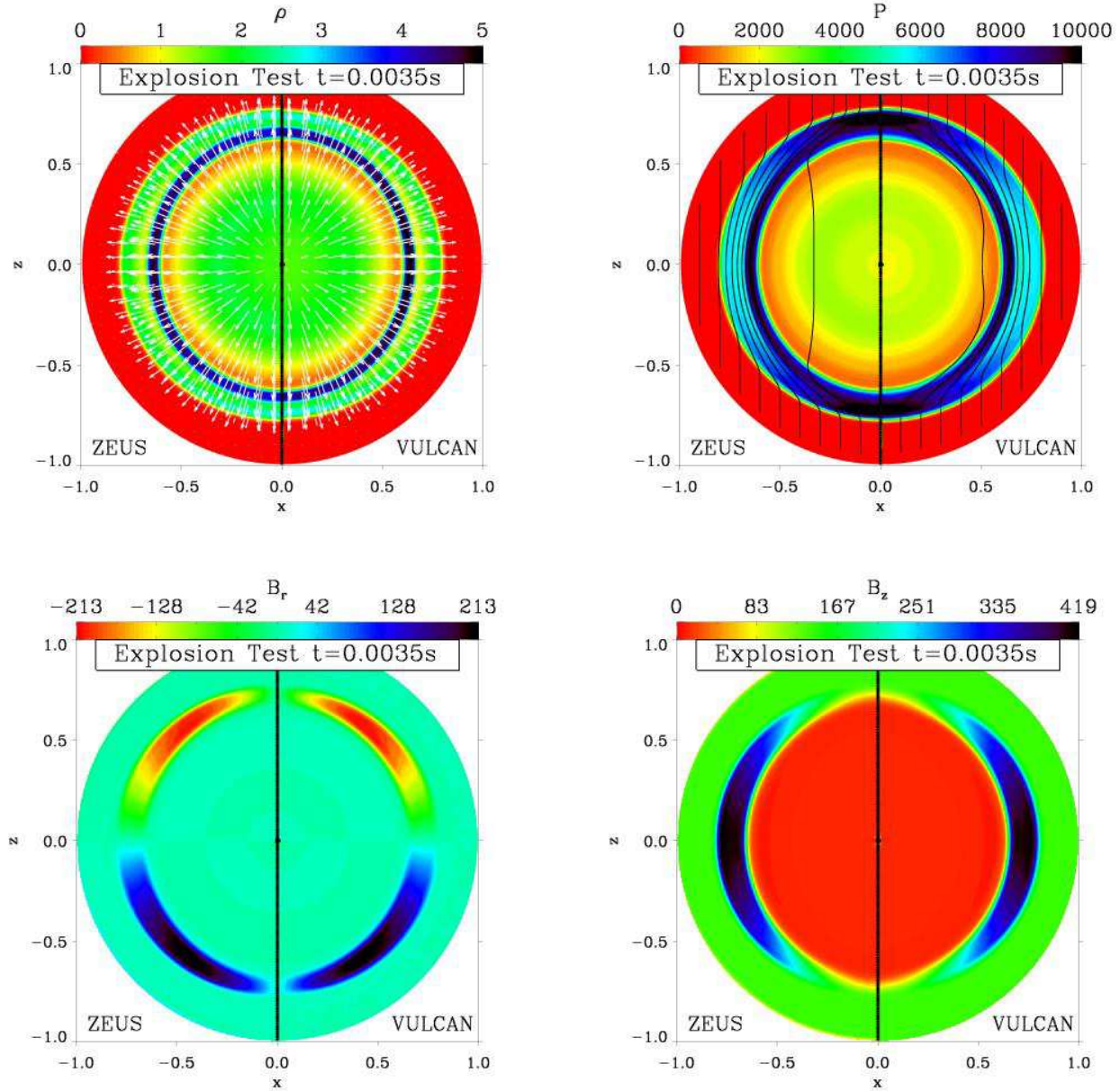


FIG. 7.— Colormaps of the high-resolution explosion test at  $t=0.035$ : density (top left), pressure (top right),  $B_r$  (bottom left) and  $B_z$  (bottom right). Each panel shows the ZEUS/2D (left) and VULCAN/2D (right) results. Velocity vectors are overlotted in white in the top-left box, with a maximum length set to 10% of the width of the panel, and a maximum magnitude of 165 (all quantities are dimensionless). Magnetic field lines are overlotted in black in the top-right box, with footpoints at  $z = -0.95r_{\max}$  equally spaced along  $x$  every  $0.1r_{\max}$ .

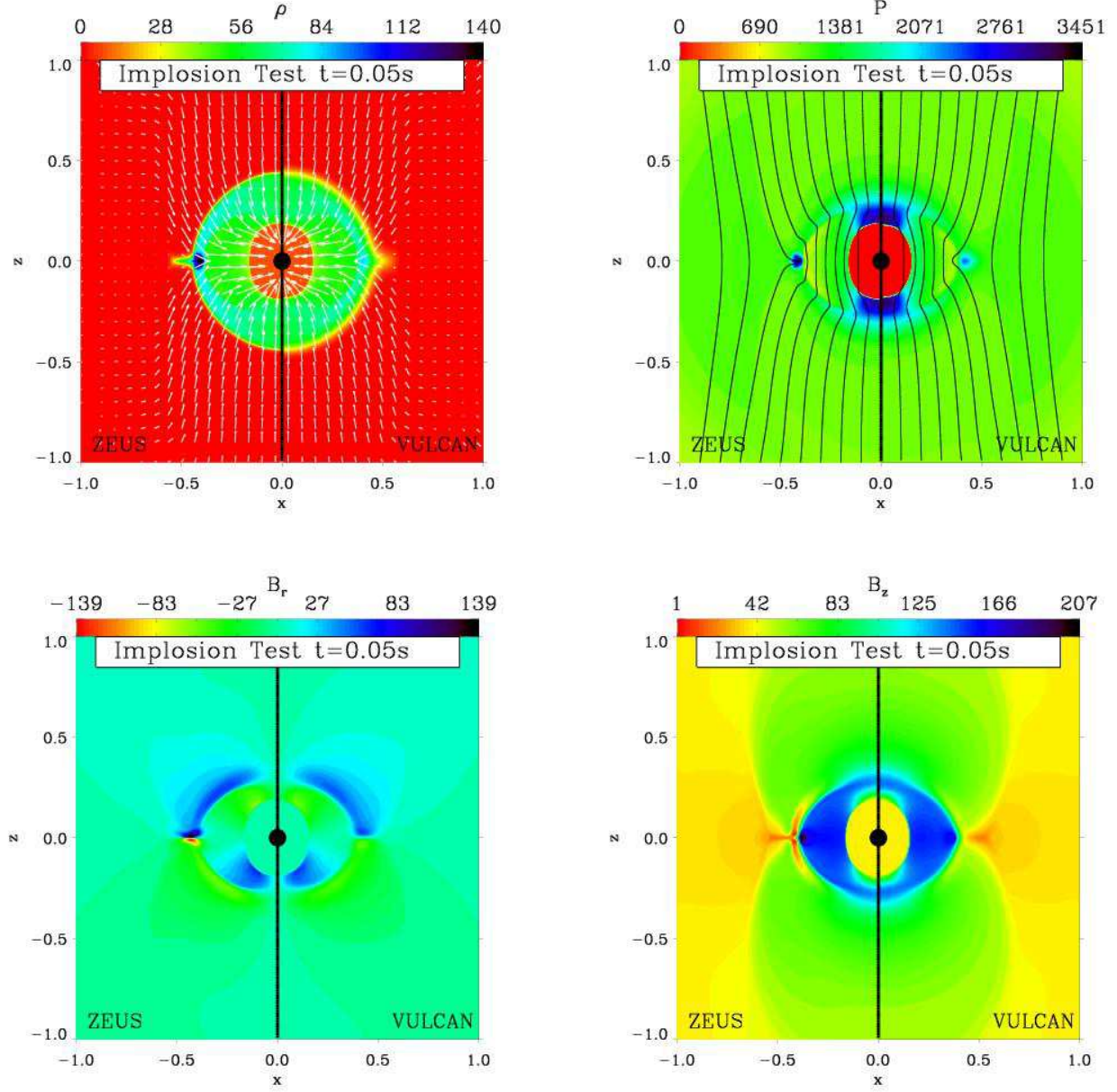


FIG. 8.— Colormaps of the high-resolution non-rotating implosion test at  $t=0.05$ , just before the shock bounces at the inner boundary: density (top left), pressure (top right),  $B_r$  (bottom left) and  $B_z$  (bottom right). Each panel shows the ZEUS/2D (left) and VULCAN/2D (right) results. Velocity vectors are overplotted in white in the top-left box, with a maximum length set to 10% of the width of the panel, and a maximum magnitude of 15 (all quantities are dimensionless). Magnetic field lines are overplotted in black in the top-right box. Note the top-bottom symmetry of the  $z$ -component of the magnetic field, and the anti-symmetry of the  $r$ -component, best rendered by the morphology of the poloidal field lines (top right panel).

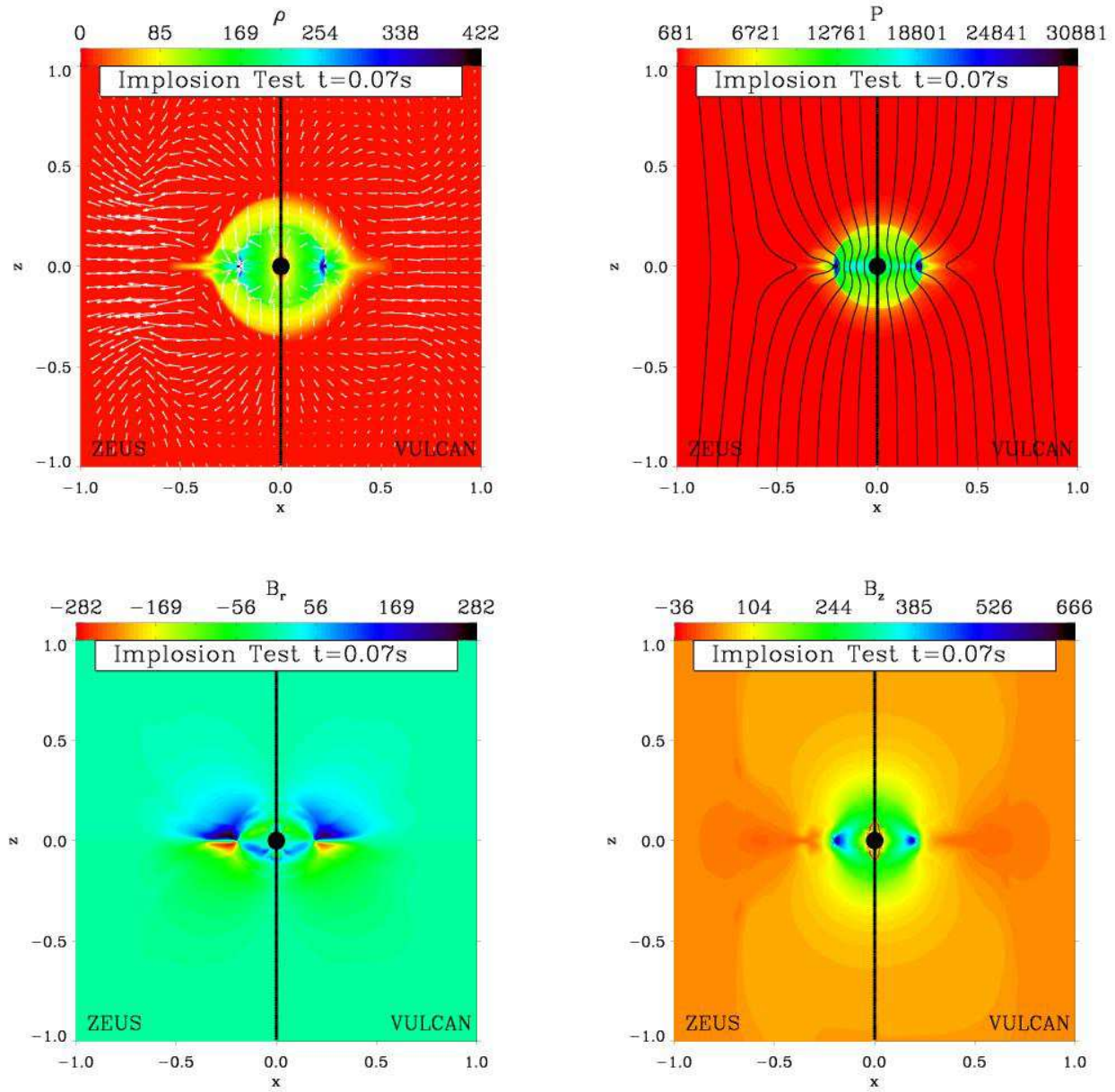


FIG. 9.— Same as Fig. 8, but at time  $t = 0.07$ , corresponding to a time after bounce of  $\sim 0.01$  seconds.

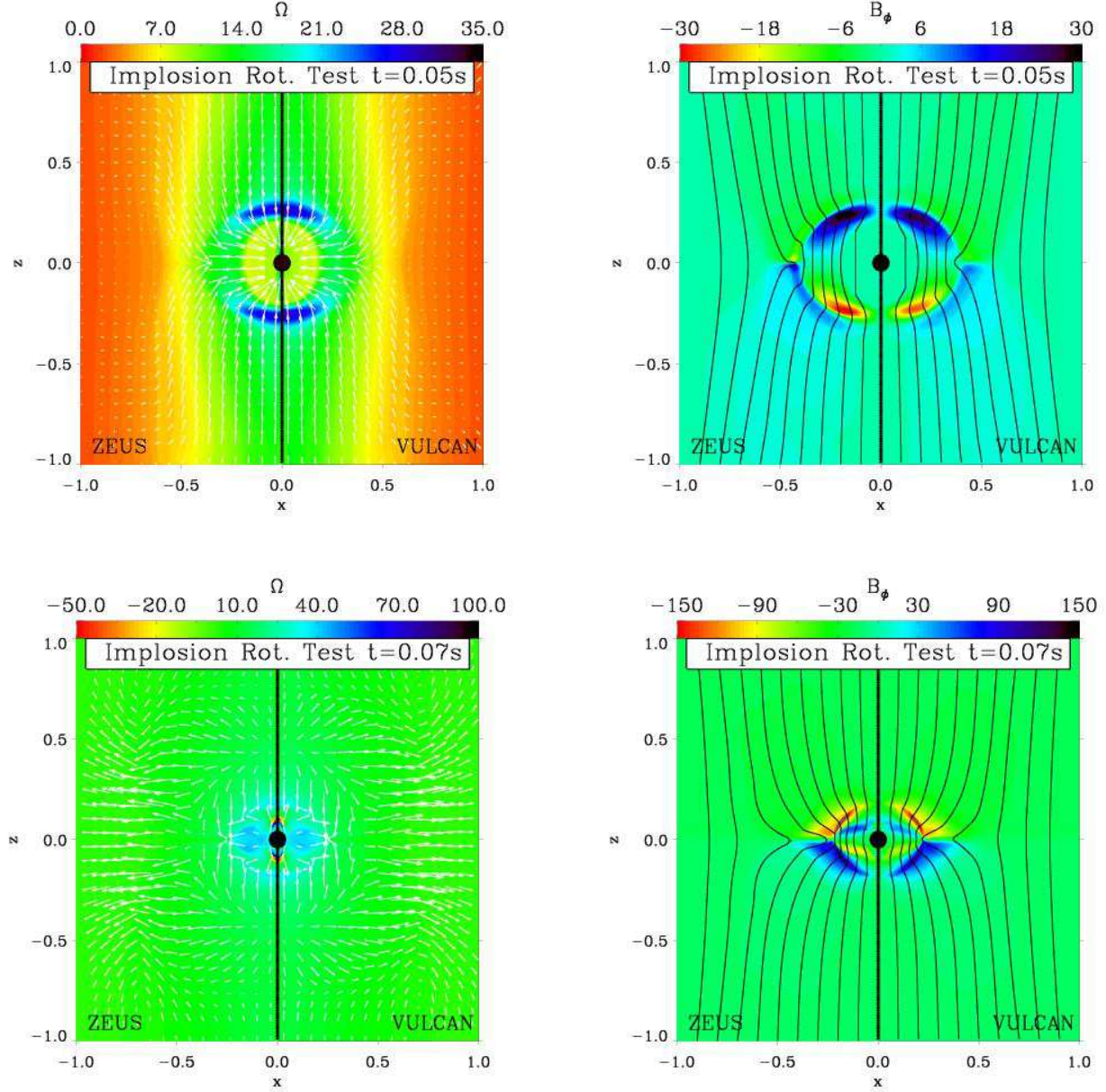


FIG. 10.— Colormaps of the rotating implosion test at  $t=0.05$  and  $t=0.07$ : The angular velocity  $\Omega$  (left column), the toroidal magnetic field  $B_\phi$  (right column), at times  $t = 0.05$  (before bounce; top row) and  $t = 0.07$  (after bounce; bottom row). Each panel shows the ZEUS/2D (left) and VULCAN/2D (right) results. Again, note the top-bottom symmetry of the  $z$ -component of the magnetic field and the anti-symmetry of the  $r$ -component, best rendered by the morphology of the poloidal field lines (right panels).

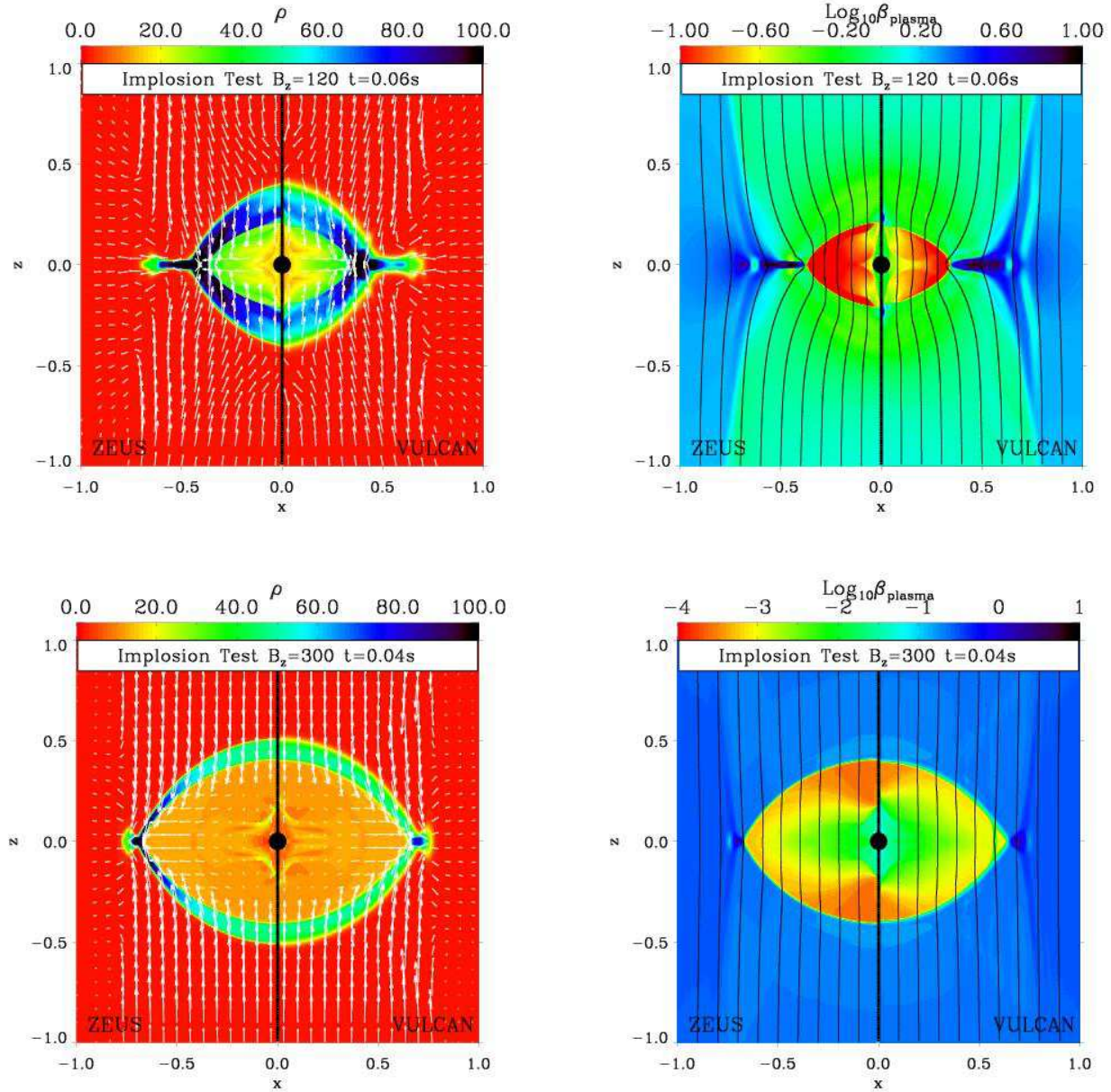


FIG. 11.— Colormaps of the high-resolution non-rotating implosion tests with dominant initial magnetic fields ( $B_z = 120$ ,  $t = 0.06$ , top row;  $B_z = 300$ ,  $t = 0.04$ , bottom row). Shown are the density (left column) and the quantity  $\beta_{\text{plasma}} = P/(B^2/8\pi)$  (right column). Each panel shows results for the ZEUS/2D (left) and VULCAN/2D (right). Again, note the top-bottom symmetry of the  $z$ -component of the magnetic field and the anti-symmetry of the  $r$ -component, best rendered by the morphology of the poloidal field lines (right panels).